

# Mechanical Models For Planar Single- and Dual-Axis MEMS Accelerometers

Ruiheng Su<sup>1,\*</sup>

<sup>1</sup>Engineering Physics, The University of British Columbia, Vancouver, BC, V6T 1Z4

\*ruihengsu@student.ubc.ca

## ABSTRACT

Microelectromechanical systems (MEMS) are ubiquitous in our daily lives. The MEMS accelerometer is used in tablets to detect device orientation, and in cars to detect collisions so airbags can be deployed. In this report, we developed mechanical models for a single- and dual-axis accelerometer attached to a planar rigid body using Lagrangian mechanics. By solving the associated Euler-Lagrange equations, we gained insight into how the damping coefficient and the natural frequency affect the accelerometer's linear operating range, sensitivity, and recovery time.

## 1 Introduction

MEMS accelerometers are miniature mechanical devices made on silicon wafers (figure 1) and protected by an encapsulation known as the packaging. By attaching this device to a body, we can extract information about the body's acceleration. This is done by measuring the displacement from equilibrium of a piece of suspended silicon, known as the proof mass.

Two common approaches to designing an accelerometer that can measure three-dimensional acceleration are

1. using three single-axis accelerometers, orthogonally oriented relative to each other<sup>1</sup>,
2. using one single-axis accelerometer to measure acceleration in the  $z$ -direction, and one dual-axis accelerometer for sensing accelerations in the  $xy$ -plane<sup>1</sup>.

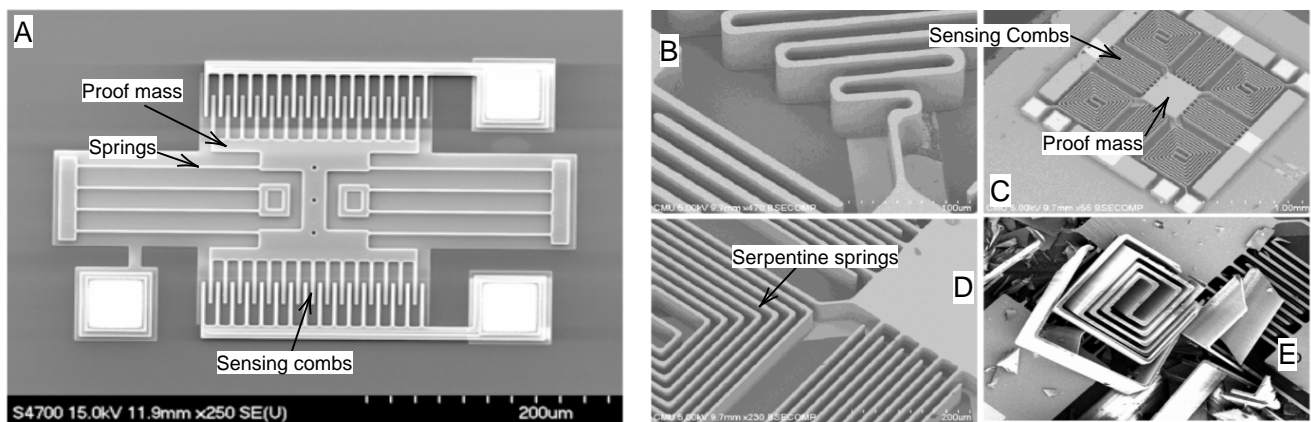


**Figure 1.** Scanning electron micrographs of a single-axis<sup>2</sup> (A) and dual-axis<sup>3</sup> (B, C, D, E) MEMS capacitive accelerometer. (A): Four polysilicon “springs” suspends an I-shaped proof mass between two vertical anchors. The proof mass is confined to oscillate vertically. (C): Four serpentine springs suspend the rectangular proof mass of the dual-axis accelerometer, granting the proof mass an additional degree of freedom.

In this report, we modelled a single- and dual-axis accelerometer using Lagrangian mechanics. Using these models, we can predict the motion of the proof mass when the accelerometers are subjected to different excitations, at different parameter combinations, providing insight into how design parameters can be optimized.

## 2 Method

### 2.1 Damping

Mechanical damping and friction violate the conservation of energy. To account for mechanical damping in our systems, we modified the Euler-Lagrange equations to include a dissipative term - as outlined by Landau and Lifshitz:

$$\frac{d}{dt} \left( \frac{\partial \mathcal{L}}{\partial \dot{q}_i} \right) = \frac{\partial \mathcal{L}}{\partial q_i} - \frac{\partial \mathcal{F}}{\partial \dot{q}_i}, \quad (1)$$

where  $\mathcal{F}$  is a function of the generalized velocities  $\dot{q}_i$ , called the dissipative function<sup>4</sup>.

In general, the dissipative function is a positive definite quadratic form related to the energy loss of the system<sup>4</sup>.

$$\mathcal{F} = \frac{1}{2} \sum_{i,k} \alpha_{ik} \dot{q}_i \dot{q}_k. \quad (2)$$

### 2.2 Single-axis

We approximated the single-axis accelerometer as an 1-D damped oscillator, as described in figure 2.

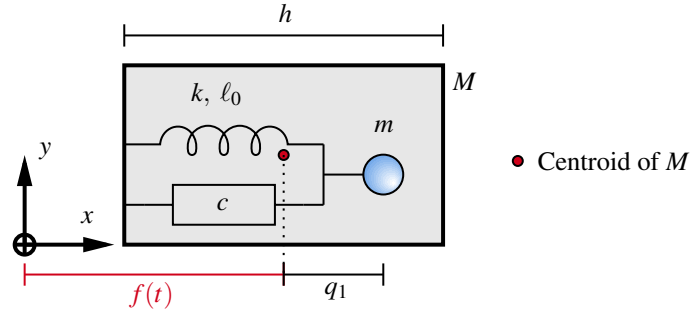


**Figure 2.** Model for the single-axis accelerometer. The I-shaped proof mass was modelled as a point mass  $m$ . The packaging of the accelerometer was modelled as a rectangular rigid body  $M$ , of width  $h$ . Both  $m$  and  $M$  are confined to moving along the  $x$ -axis. The location of the centroid of  $M$  was specified by a function  $f(t)$ . Damping was specified by a constant  $c$ . The problem has a single degree of freedom,  $q_1$ , representing the displacement of  $m$  away from the centroid of  $M$ .

The kinetic energy of the system was equal to the kinetic energy of proof mass only. We neglected the kinetic energy of packaging since it does not depend on the generalized coordinates.

$$T = \frac{1}{2} m \left( \frac{d}{dt} (f(t) + q_1) \right)^2 = \frac{1}{2} m (2\dot{f}\dot{q}_1 + \dot{q}_1^2). \quad (3)$$

Since the system is confined along the  $x$ -axis, we only considered the potential energy of the spring. The length of the spring is given by  $\ell = q_1 + h/2$ . We took the unstretched length of the spring to be  $\ell_0 = h/2$ .

The Lagrangian was

$$\mathcal{L} = T - U = \frac{1}{2} m (2\dot{f}\dot{q}_1 + \dot{q}_1^2) = \frac{1}{2} m (2\dot{f}\dot{q}_1 + \dot{q}_1^2) - \frac{1}{2} k q_1^2. \quad (4)$$

We chose the dissipative function to be

$$\mathcal{F} = \frac{c}{2} \dot{q}_1^2. \quad (5)$$

A single degree of freedom results in one Euler-Lagrange equation. After simplification, our Euler-Lagrange equation was:

$$\ddot{f} + \ddot{q}_1 = -\omega_0^2 q_1 - 2\lambda \dot{q}_1, \quad (6)$$

where  $\omega_0 = \sqrt{k/m}$  is the natural frequency of the accelerometer,  $c/m = 2\lambda$ , and  $\lambda$  is known as a damping coefficient<sup>4</sup> with units of frequency.

Rearranging equation (6) resulted in the familiar second order, linear, ordinary differential equation for a damped harmonic oscillator:

$$\ddot{q} + 2\lambda\dot{q} + \omega_0^2 q = -\ddot{f}. \quad (7)$$

### 2.2.1 Motions Considered

We considered two types of motions of the accelerometer packaging, with

$$k \in \{1, 25, 100\}; \quad \lambda \in \{0.5, 2.5, 5\} \quad m = 1; \quad h = 1; \quad d = 0.3.$$

**Sinusoidal:**  $f_1(t) = F \sin(\gamma t)$ , where  $F \geq 0$ , and  $\gamma$  is the forcing frequency. We solved this type of forcing analytically with  $F = 1$ .

**Polynomial:** The second type models the motion of an accelerometer attached to a automobile. The automobile starts at  $x = 0$ , accelerates, then decelerates to a stop at  $x = 1$ . It is a ratio of polynomials:

$$f_2(t) = \frac{At^4}{t^4 + 1} \quad A = 1 \text{ [m]}. \quad (8)$$

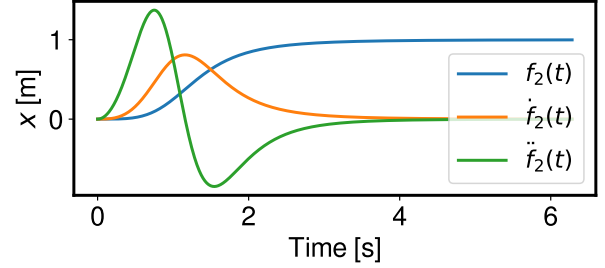


**Figure 3.** Plot of  $f_2, \dot{f}_2, \ddot{f}_2$ .  $f_2(t)$  approaches 1 for large  $t$ .

For both cases, we considered  $m$  to begin at rest, coinciding with the centroid of  $M$ .

### 2.2.2 Solution methods

**Sinusoidal:** The general solutions second order, linear, inhomogeneous, ordinary differential equations is the sum of a homogeneous solution and a particular solution. To find the particular solution to equation (7), we used the method of complex exponentials<sup>5</sup>. We confirmed the correctness of our analytical solution by also approximating the solution numerically.

**Polynomial:** We used a combination of the `Scipy`, `Sympy`, and `Numpy` packages in `Python 3.8.5` to find approximate solutions. The general logic is present in figure 4. The generality of our method helped us to solve equation (7) for other types of forcing with little modification.

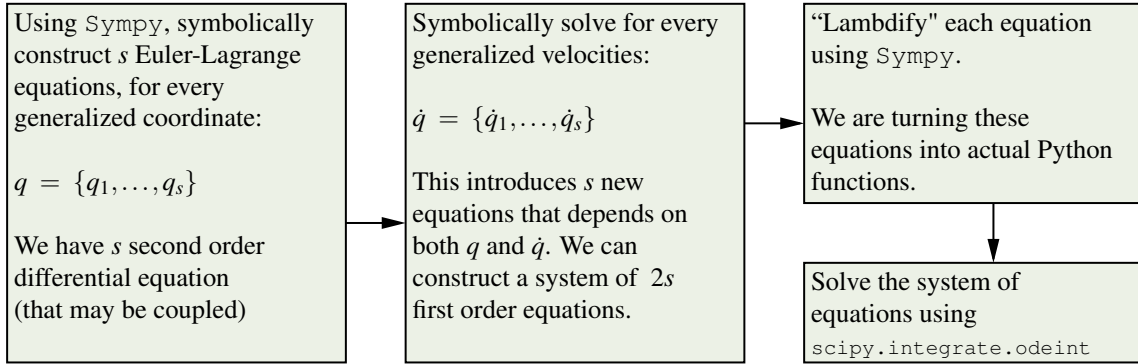


**Figure 4.** The general recipe used to solve coupled second order differential equations in `Python`.

## 2.3 Dual-axis

Our model for the planar dual-axis accelerometer is described in figure 5.

Since the motion of  $M$  is completely specified by known functions  $(f, g, \theta)$ , we discarded the kinetic energy of  $M$ . The kinetic energy had the general form

$$T = \frac{1}{2}mv_{\text{cm}}^2 + \frac{1}{2}\Omega_z^2 I_{zz}^{\text{cm}}, \quad (9)$$

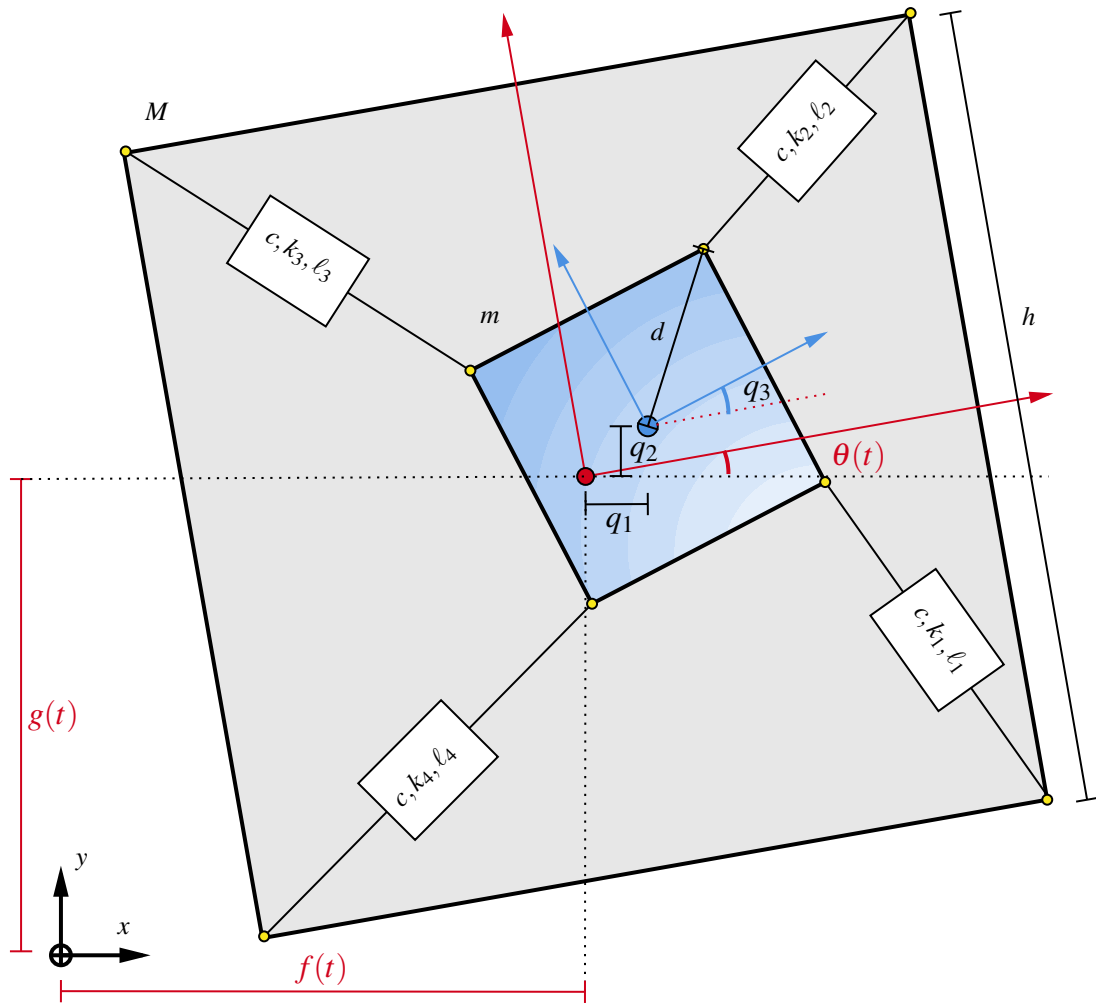


**Figure 5.** Model for the dual-axis accelerometer. We modelled the proof mass as a rigid, homogeneous square of diagonal length  $d$ , and mass  $m$ . The packaging of the accelerometer was modelled as a square of width  $h$  and mass  $M$ . The four serpentine springs were converted to four linear springs of spring constant  $k_j$ ,  $j = 1, 2, 3, 4$ , and unstretched lengths equal to  $(h/\sqrt{2}) - d$ . Damping was specified by a constant  $c$ . At any time, the coordinates of centroid of  $M$  in the inertial reference frame (IRF) was specified by  $[f(t) \ g(t)]^T$ . The orientation of  $M$  relative to the  $x$ -axis was specified by  $\theta(t)$ . The problem has three degrees of freedom, indicated by  $\underline{q} = [q_1 \ q_2 \ q_3]^T$ .

where  $v_{cm}$  is the speed of the centroid of  $m$  (indicated by the blue dot in figure 5),  $\Omega_z$  is the angular frequency, and  $I_{zz}^{cm}$  is the moment of inertia about  $z$ -axis.

The coordinate of the proof mass in the IRF was

$$\underline{r}_{cm} = \begin{bmatrix} f(t) + q_1 \\ g(t) + q_2 \end{bmatrix} \quad (10)$$

The speed squared was:

$$v_{cm}^2 = 2\dot{f}\dot{q}_1 + \dot{q}_1^2 + 2\dot{g}\dot{q}_2 + \dot{q}_2^2. \quad (11)$$

About the center of mass, the moment of inertia the proof mass about  $z$  axis was

$$I_{zz}^{cm} = \frac{m}{3}d^2. \quad (12)$$

In the IRF, the orientation of the proof mass was specified by  $q_3$  and  $\theta(t)$ . So

$$\Omega_z^2 = \left( \frac{d}{dt} (q_3 + \theta(t)) \right)^2 \rightarrow \dot{q}_3^2 + 2\dot{\theta}\dot{q}. \quad (13)$$

All together, the kinetic energy of the system was

$$T = \frac{1}{2}m(2\dot{f}\dot{q}_1 + \dot{q}_1^2 + 2\dot{g}\dot{q}_2 + \dot{q}_2^2) + \frac{1}{2}(\dot{q}_3^2 + 2\dot{\theta}\dot{q}) \frac{m}{3}d^2. \quad (14)$$

The potential energy of the system consists of four spring energy terms.

$$U(q_1, q_2, q_3) = \frac{1}{2} \sum_{j=1}^4 k_j \left( \ell_j - \left( \frac{h}{\sqrt{2}} - d \right) \right)^2. \quad (15)$$

The main challenge in constructing the potential energy was to write the position of the vertices of the proof mass and the packaging in the IRF.

Let  $\underline{\alpha}_j$  be the position of the  $j^{\text{th}}$  vertex on the proof mass,  $\underline{\beta}_j$  be the position of the  $j^{\text{th}}$  vertex on the packaging, such that spring  $k_j$  connects vertices  $\underline{\alpha}_j$  and  $\underline{\beta}_j$ , and  $\ell_j = \|\underline{\alpha}_j - \underline{\beta}_j\|$ . We determined that

$$\underline{\alpha}_1 = r_{\text{cm}} + d \begin{bmatrix} \cos(\pi/4 - (\theta + q_3)) \\ -\sin(\pi/4 - (\theta + q_3)) \end{bmatrix} \quad \underline{\beta}_1 = \begin{bmatrix} f(t) \\ g(t) \end{bmatrix} + \frac{h}{\sqrt{2}} \begin{bmatrix} \cos(\pi/4 - \theta) \\ -\sin(\pi/4 - \theta) \end{bmatrix} \quad (16)$$

$$\underline{\alpha}_2 = r_{\text{cm}} + d \begin{bmatrix} \cos(\pi/4 + (\theta + q_3)) \\ \sin(\pi/4 + (\theta + q_3)) \end{bmatrix} \quad \underline{\beta}_2 = \begin{bmatrix} f(t) \\ g(t) \end{bmatrix} + \frac{h}{\sqrt{2}} \begin{bmatrix} \cos(\pi/4 + \theta) \\ \sin(\pi/4 + \theta) \end{bmatrix} \quad (17)$$

$$\underline{\alpha}_3 = r_{\text{cm}} + d \begin{bmatrix} -\sin(\pi/4 + (\theta + q_3)) \\ \cos(\pi/4 + (\theta + q_3)) \end{bmatrix} \quad \underline{\beta}_3 = \begin{bmatrix} f(t) \\ g(t) \end{bmatrix} + \frac{h}{\sqrt{2}} \begin{bmatrix} -\sin(\pi/4 + \theta) \\ \cos(\pi/4 + \theta) \end{bmatrix} \quad (18)$$

$$\underline{\alpha}_4 = r_{\text{cm}} - d \begin{bmatrix} \sin(\pi/4 - (\theta + q_3)) \\ \cos(\pi/4 - (\theta + q_3)) \end{bmatrix} \quad \underline{\beta}_4 = \begin{bmatrix} f(t) \\ g(t) \end{bmatrix} - \frac{h}{\sqrt{2}} \begin{bmatrix} \cos(\pi/4 + \theta) \\ \sin(\pi/4 + \theta) \end{bmatrix}. \quad (19)$$

The Lagrangian was

$$\mathcal{L} = T - U = \frac{1}{2}m(2\dot{f}\dot{q}_1 + \dot{q}_1^2 + 2\dot{g}\dot{q}_2 + \dot{q}_2^2) + \frac{1}{2}(\dot{q}_3^2 + 2\dot{\theta}\dot{q}) \frac{m}{3}d^3 - \frac{1}{2} \sum_{j=1}^4 k_j \left( \ell_j - \left( \frac{h}{\sqrt{2}} - d \right) \right)^2. \quad (20)$$

We chose the dissipative function associated with the  $j^{\text{th}}$  spring to be

$$\mathcal{F}_j = \frac{c}{2} \dot{\ell}_j^2. \quad (21)$$

The three Euler-Lagrange equation took the form:

$$\frac{d}{dt} \left( \frac{\partial \mathcal{L}}{\partial \dot{q}_i} \right) = \frac{\partial \mathcal{L}}{\partial q_i} - \sum_{j=1}^4 \frac{d\mathcal{F}_j}{dq_i}. \quad (22)$$

### 2.3.1 Motions Considered

We considered three types of motion for the packaging, with

$$k_i = 10, i = 1, 2, 3, 4; \quad \lambda = 0 \quad m = 1; \quad h = 1; \quad d = 0.3.$$

So the natural frequency of the system was  $\omega_0 = \sqrt{10}$  Hz.

**Stationary:**  $f(t) = g(t) = 0, \theta(t) = 0$  for all  $t$ .

We solved for the motion of a proof mass starting at rest, at different positions from the centroid of the packaging.

**Revolving:**  $f(t) = F \cos(\gamma t), g(t) = g_0 \sin(\gamma t), \theta(t) = 0$  for all  $t$ .

We chose  $F = g_0 = 1$ , and  $\gamma = 1$ . We considered the proof mass at rest, at  $q_1 = 0, q_2 = 0, q_3 = 0$ .

**Revolving and spinning:**  $f(t) = F \cos(\gamma t)$ ,  $g(t) = g_0 \sin(\gamma t)$ ,  $\theta(t) = t/2\pi$ .  $g(t) = g_0 \sin(\gamma t)$ ,  $\theta(t) = 0$  for all  $t$ .

We chose  $F = g_0 = 1$ ,  $\gamma = 1$  and  $\gamma = 5$ . The proof mass began rest, at  $q_1 = 0$ ,  $q_2 = 0$ ,  $q_3 = 0$ .

### 2.3.2 Solution methods

We solved the Euler Lagrange equations for the three types of motion numerically, as described in figure 4.

## 3 Result

### 3.1 Single-axis

#### 3.1.1 Sinusoidal:

The solutions to equation (7) with  $f_1 = F \sin(\gamma t)$ ,  $-\ddot{f}_1 = \gamma^2 F \sin(\gamma t)$  are well known<sup>4,5</sup>. Depending on the values of  $\omega_0$  and  $\lambda$ , the homogeneous solutions belonged to one of the three following cases, up to constants  $A, B$ . When  $\lambda^2 > \omega_0^2$ , the system is said to be overdamped:

$$q_{1h} = A e^{-(\lambda + \sqrt{\lambda^2 - \omega_0^2})t} + B e^{-(\lambda - \sqrt{\lambda^2 - \omega_0^2})t}. \quad (23)$$

Critical damping occurs when  $\lambda^2 = \omega_0^2$ :

$$q_{1h} = (A + Bt) e^{-\lambda t}. \quad (24)$$

Underdamping occurs when  $\lambda^2 < \omega_0^2$ :

$$q_{1h} = e^{-\lambda t} \left( A \sin \left( \sqrt{\omega_0^2 - \lambda^2} t \right) + B \cos \left( \sqrt{\omega_0^2 - \lambda^2} t \right) \right). \quad (25)$$

The particular solution is independent of the initial conditions. Using the method of complex exponentials, we found the particular solution to be

$$q_{1p} = A(\omega_0, \lambda; \gamma) \sin(\gamma t - \phi), \quad (26)$$

where the amplitude is

$$A(\omega_0, \lambda; \gamma) = \frac{\gamma^2 F}{\sqrt{(\omega_0^2 - \gamma^2)^2 + (2\lambda\gamma)^2}}, \quad (27)$$

and the phase is given by the argument of  $(\omega_0^2 - \gamma^2) + i2\lambda\gamma$

$$\phi = \arg((\omega_0^2 - \gamma^2) + i2\lambda\gamma); \quad \phi(t) \in [0, 2\pi). \quad (28)$$

For  $F = 1$ ,  $q_1 = 0$ ,  $\dot{q}_1 = 0$ , we found coefficients  $A, B$  for the overdamped case to be

$$A = -B - q_{1p}(0); \quad (29)$$

$$B = \frac{\dot{q}_{1p}(0) + (\lambda + \sqrt{\lambda^2 - \omega_0^2}) q_{1p}(0)}{-2\sqrt{\lambda^2 - \omega_0^2}}. \quad (30)$$

We found for the critically damped case:

$$A = -q_{1p}(0); \quad (31)$$

$$B = \lambda A - \dot{q}_{1p}(0). \quad (32)$$

And we found for the underdamped case:

$$A = \frac{\lambda B - \dot{q}_{1p}(0)}{\sqrt{\omega_0^2 - \lambda^2}}; \quad (33)$$

$$B = -q_{1p}(0). \quad (34)$$

If  $\lambda > 0$ ,  $q_{1h}$  tends to zero for large  $t$  due to the exponential factor, regardless of the initial conditions. So the particular solution is also the steady-state solution.

The first derivative of equation (27) with respect to  $\gamma$  is

$$\frac{d}{d\gamma}A(\omega_0, \lambda; \gamma) = \frac{2F\gamma(2\gamma^2\lambda^2 - \gamma^2\omega_0^2 + \omega_0^4)}{(\gamma^4 + 4\gamma^2\lambda^2 - 2\gamma^2\omega_0^2 + \omega_0^4)^{\frac{3}{2}}}, \quad (35)$$

which has three roots. The first root is at  $\gamma_1 = 0$ . The second and third roots are

$$\gamma_2 = -\sqrt{\frac{\omega_0^4}{\omega_0^2 - 2\lambda^2}} \quad (36)$$

and

$$\gamma_3 = \sqrt{\frac{\omega_0^4}{\omega_0^2 - 2\lambda^2}}. \quad (37)$$

We see that the single-axis system has a resonance frequency,  $\gamma = \gamma_3$  if and only if  $\omega_0^2 - 2\lambda^2 > 0$ . Figures 6 and 7 illustrates the single-axis system at resonance, for specified combinations of  $\omega_0$  and  $\lambda$ .

When  $\gamma$  is large compared to  $\omega_0$  - this represents a rapidly moving packaging - the steady-state amplitude (given by equation (27)) tends to the amplitude of  $f_1(t)$ , which happens to be 1. This limiting behaviour was made clear by dividing the numerator and denominator by  $\gamma^2$ .

$$\lim_{\gamma \rightarrow \infty} A(\omega_0, \lambda; \gamma) = \lim_{\gamma \rightarrow \infty} \frac{F}{\sqrt{(\omega_0^2/\gamma^2 - 1)^2 + (2\lambda)^2/\gamma^2}} = F. \quad (38)$$

When  $\omega_0$  is large compared to  $\gamma$  - this represents an accelerometer with hard springs, or a heavy proof mass - the steady-state amplitude tends to  $F(\gamma/\omega_0)^2$ . To see this behaviour for large  $\omega_0$ , we divided the numerator and denominator by  $\omega_0^2$ .

$$\lim_{\omega_0 \rightarrow \infty} A(\omega_0, \lambda; \gamma) = \frac{F(\gamma/\omega_0)^2}{\sqrt{(1 - \gamma^2/\omega_0^2)^2 + (2\lambda\gamma)^2/\omega_0^4}} = F\left(\frac{\gamma}{\omega_0}\right)^2. \quad (39)$$

And  $\phi$  approaches 0 for large  $\omega_0 \gg \gamma$ :

$$\lim_{\omega_0 \rightarrow \infty} \phi = \lim_{\omega_0 \rightarrow \infty} \arg((\omega_0^2 - \gamma^2) + i2\lambda\gamma) = 0,$$

When a single-axis accelerometer is designed with a natural frequency much larger than its forcing frequency, the displacement amplitude of proof mass from equilibrium can be approximated by

$$q_{1p} \approx F\left(\frac{\gamma}{\omega_0}\right)^2 \sin(\gamma t). \quad (40)$$

### 3.1.2 Polynomial:

The phase portraits for  $q_1 = q_{1h} + q_{1p}$  for various combination of  $\omega_0, \lambda$  are shown in figure 8.

## 3.2 Dual-axis

### 3.2.1 Stationary:

The approximated trajectories for the proof mass starting at rest, at under different initial positions are shown in figure 9. A video animation can also be found on YouTube:

<https://www.youtube.com/watch?v=D2rm0ejzofY>

### 3.2.2 Revolving:

The phase portraits of the generalized coordinates when  $\gamma = 1$  are shown in figure 10.

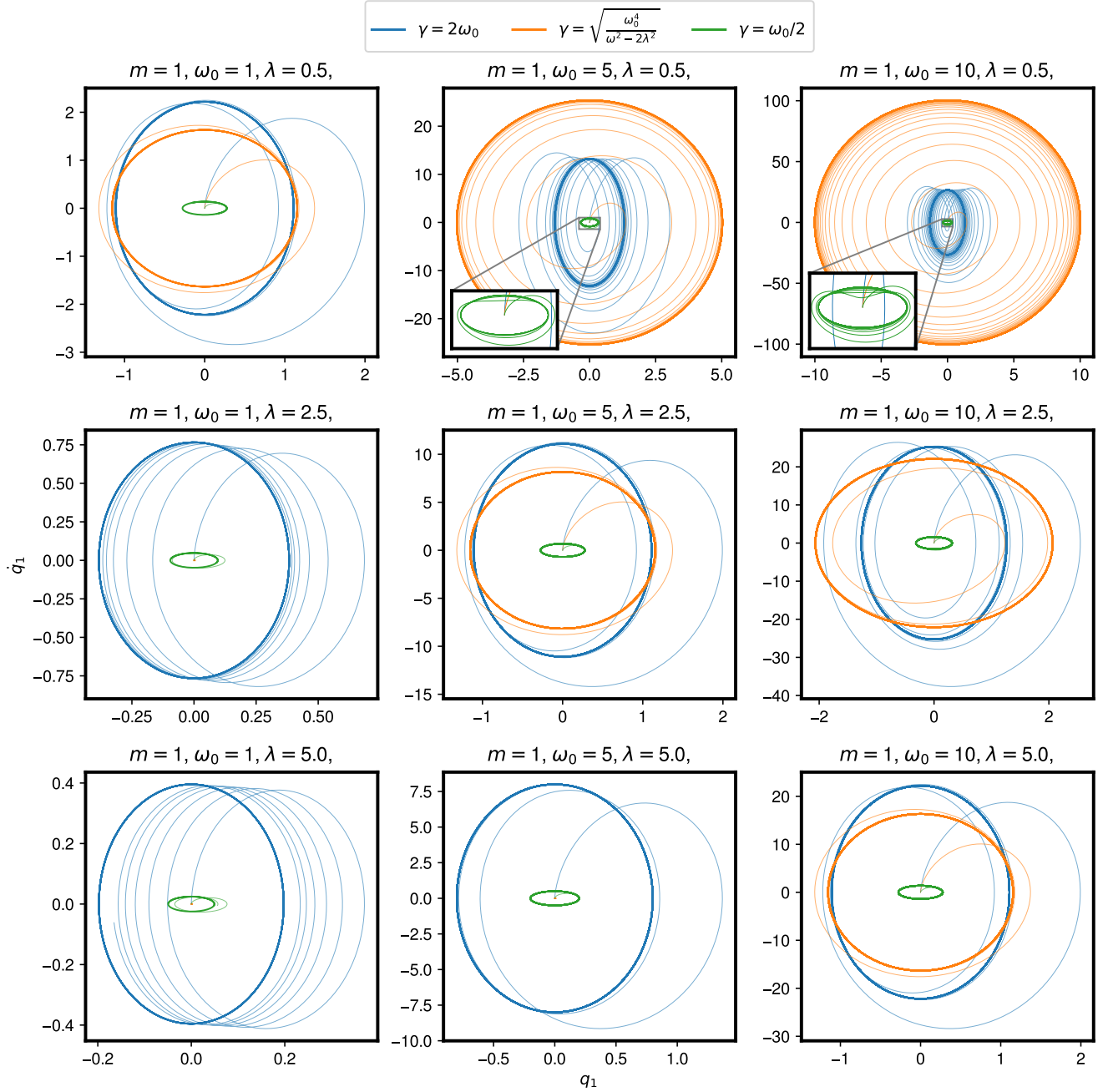


**Figure 6.** Phase portraits of the single-axis accelerometer for various combinations of natural frequency  $\omega_0$ , and damping coefficient  $\lambda$ , for  $t \in [0, 6\pi]$ , under sinusoidal excitation  $f_1(t) = F \sin(\gamma t)$ ,  $F = 1$ . For each combination, we considered  $\gamma$  at double the natural frequency (in blue), at resonance (in orange), and at half the natural frequency (in green). The complete solution can be seen tending to the steady-state solution as the homogeneous solution exponentially decays.

### 3.2.3 Revolving and spinning:

The phase portraits of the generalized coordinates when  $\gamma = 1$  are shown in figure 11. Figures 10, and 11 closely resemble each other, since the dual-axis systems they describe only differ in whether the packaging was allowed to spin.

The phase portraits of the generalized coordinates when  $\gamma = 5$  are shown in figure 12. A snapshot of the accelerometer the during time evolution is shown in figure 13.



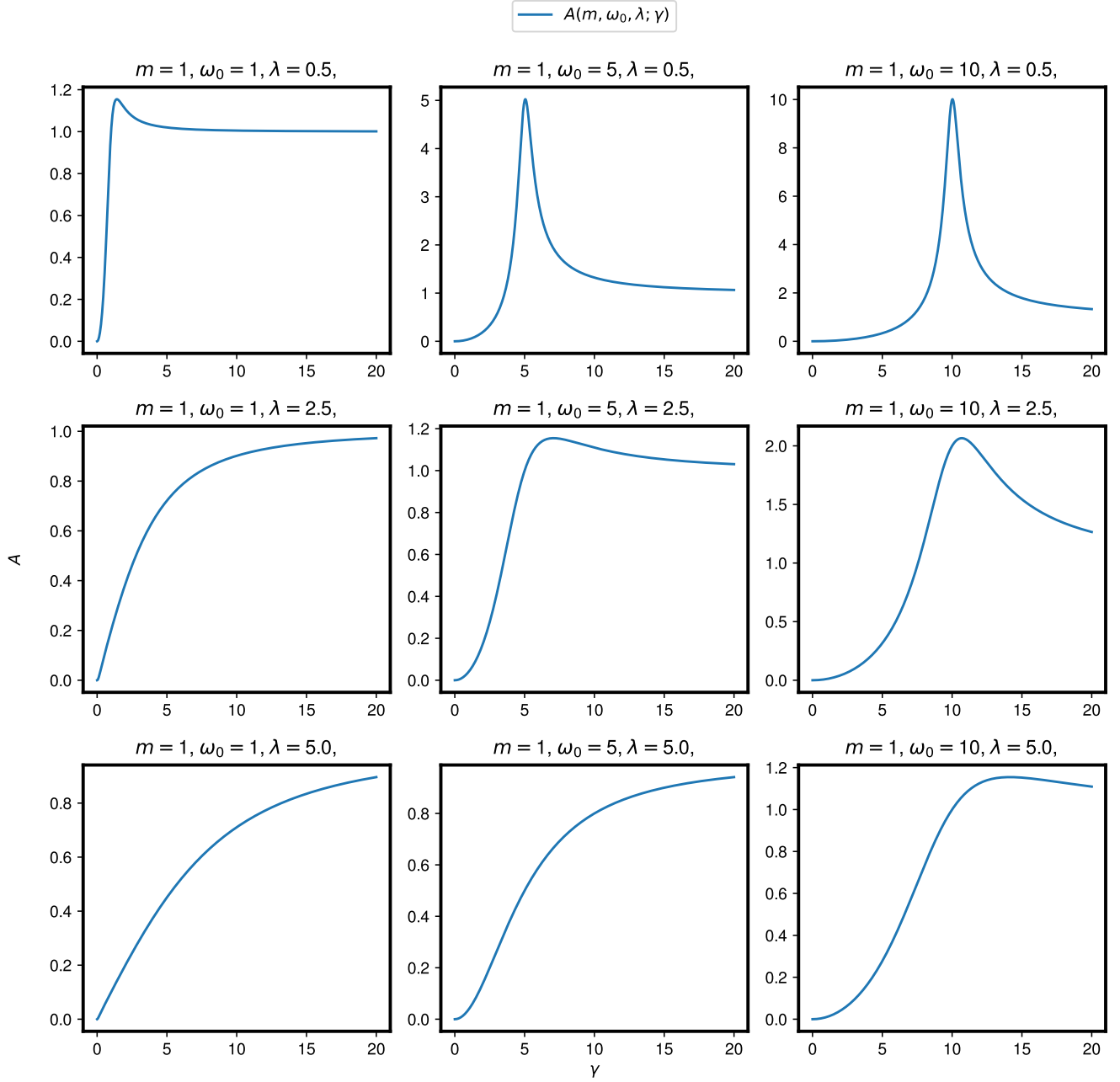


**Figure 7.** The amplitude of the steady-state solution as a function of the forcing frequency  $\gamma$ . Since not all amplitude plots show a local maximum, not all combinations of  $\omega_0$  and  $\lambda$  allows for a resonance frequency. For large  $\gamma$ , the amplitude of steady-state solution tends to the amplitude of  $f_1(t)$ , which is equal  $F = 1$ .

## 4 Discussion

Examining the behaviour of the steady-state amplitude (equation (27)) for the single-axis accelerometer when  $\omega_0 \gg \gamma$  revealed what we will call the “linearity” property of the accelerometer. When approximation by equation (40) is acceptable, we can directly “read off” of the acceleration amplitude of the packaging by measuring the displacement of the proof mass, and scaling the result by  $\omega_0^2$ .

$$A(\omega_0, \lambda; \gamma) \omega_0^2 \approx F \gamma^2 \quad (41)$$

For a given  $\lambda$  and  $\omega_0$ , we can find a maximum forcing frequency, such that if the accelerometer was driven at frequencies

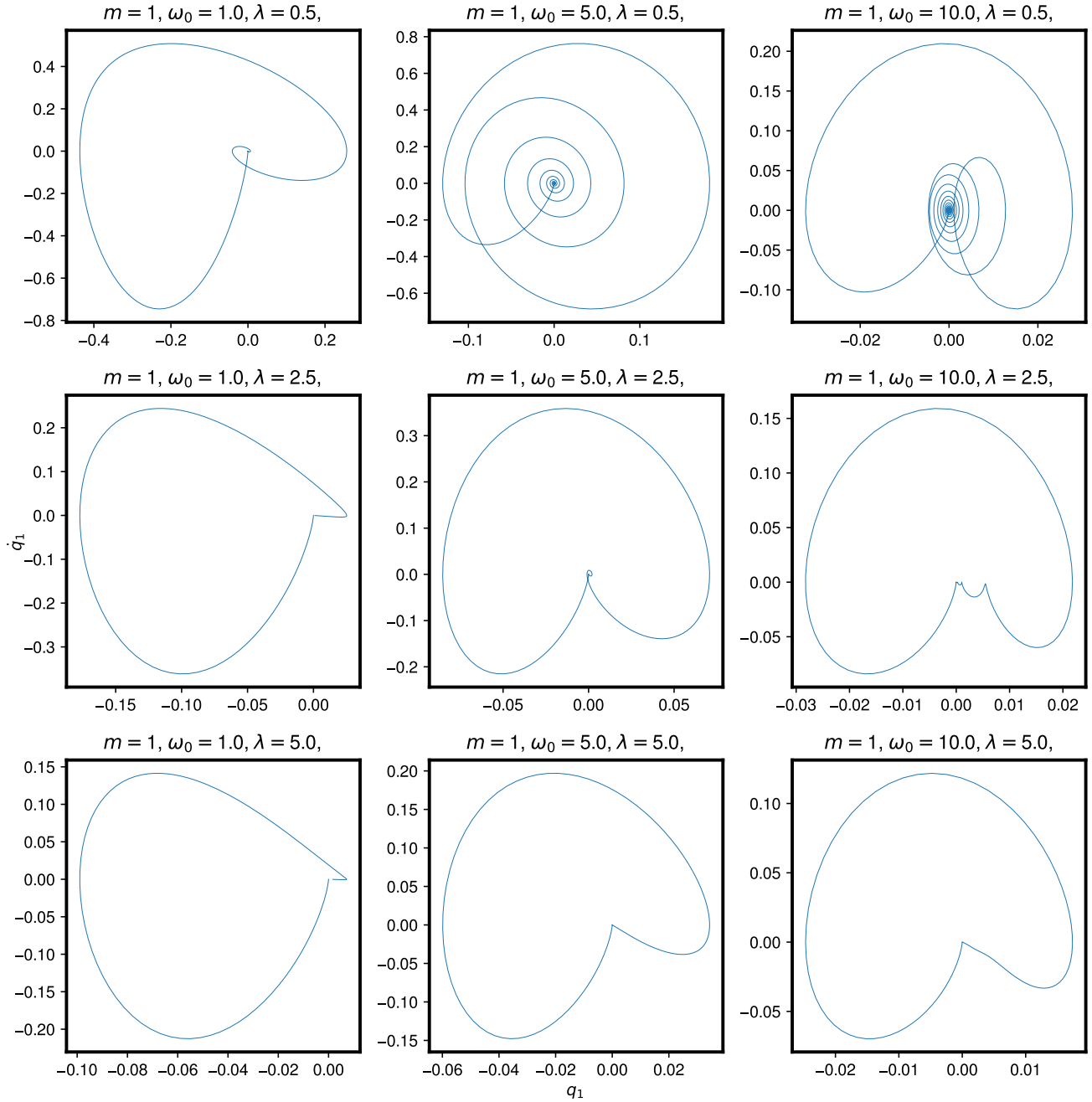


**Figure 8.** Phase portraits of the single-axis accelerometer for various combinations of natural frequency  $\omega_0$ , and damping coefficient  $\lambda$ , for  $t \in [0, 6\pi]$ , under polynomial forcing  $f_2(t) = t^4/(t^4 + 1)$ . For increasing values of  $\lambda$  relative of  $\omega_0$ , the proof mass makes more abrupt returns to equilibrium ( $q_1 = 0, \dot{q}_1 = 0$ ).

above the maximum, linearity (equations (40), (41)) no longer holds - we cannot directly measure the acceleration of the body by scaling the displacement amplitude of the proof mass.

Precisely, for some value of  $\gamma$ , we define the accelerometer to be operating linearly when the percentage error is less than a specified upper-bound,  $E \in [0, 1]$ :

$$\left| \frac{A(\omega_0, \lambda; \gamma) \omega_0^2 - \gamma^2 F}{\gamma^2 F} \right| \leq E. \quad (42)$$

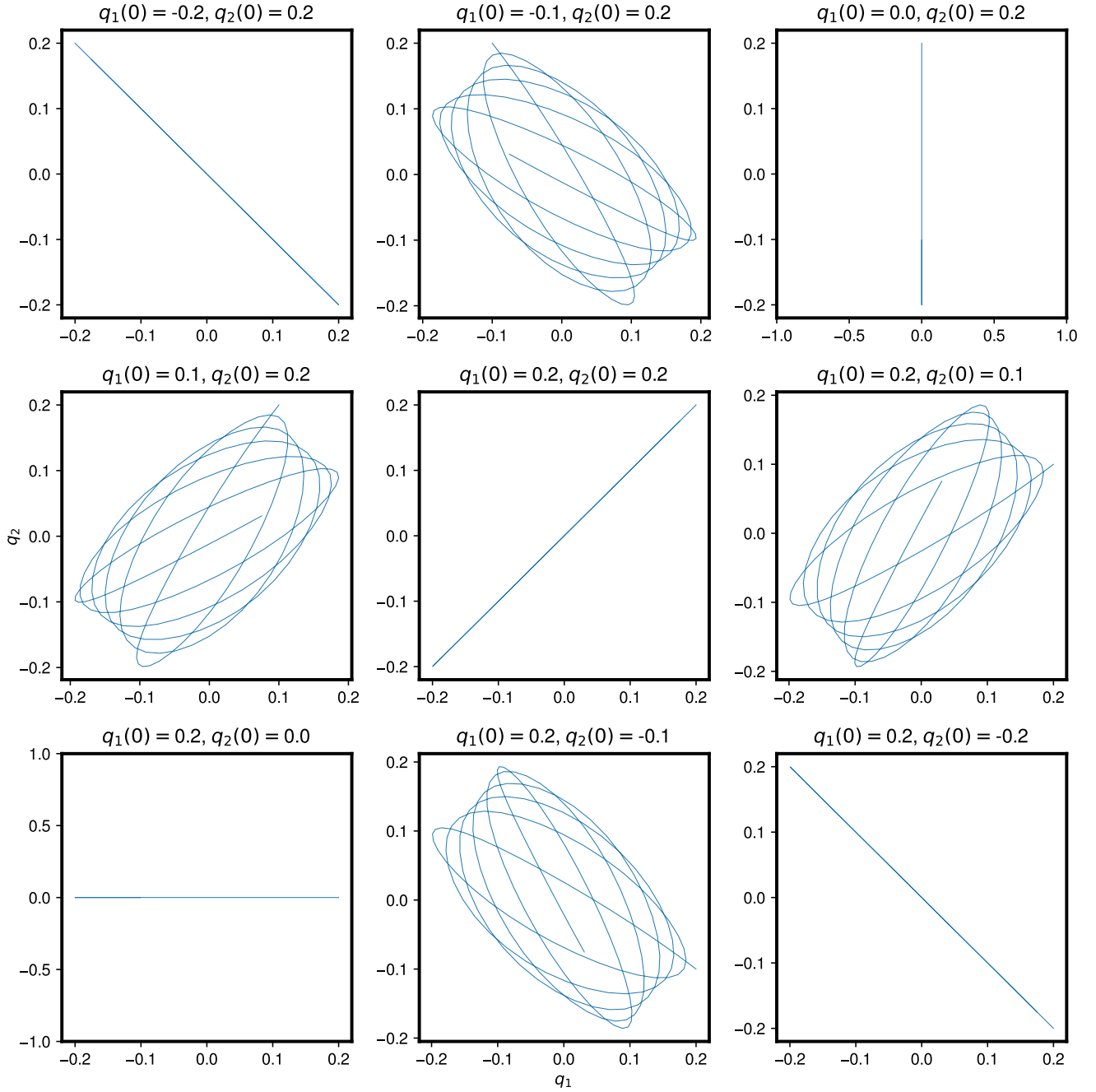


**Figure 9.** Trajectories of the center of mass of  $m$  when released from at rest, at different initial positions for  $t \in [0, 8]$ . Initial positions that where purely horizontal or vertical displacements from equilibrium resulted in purely horizontal or vertical the trajectories.

Since we expect  $A(\omega_0, \lambda; \gamma)$  to approach  $F$  for  $\gamma \gg \omega_0$  (equation (38)), the condition is equivalently:

$$\frac{\omega_0^2}{\sqrt{(\omega_0^2 - \gamma^2)^2 + (2\lambda\gamma)^2}} - 1 - E \leq 0, \quad (43)$$

Applying a series expansion to the left-hand side

$$\gamma^2 \left( -\frac{2\lambda^2}{\omega_0^4} + \frac{1}{\omega_0^2} \right) + \gamma^4 \left( \frac{6\lambda^4}{\omega_0^8} - \frac{6\lambda^2}{\omega_0^6} + \frac{1}{\omega_0^4} \right) - E + O(\gamma^6) \leq 0, \quad (44)$$

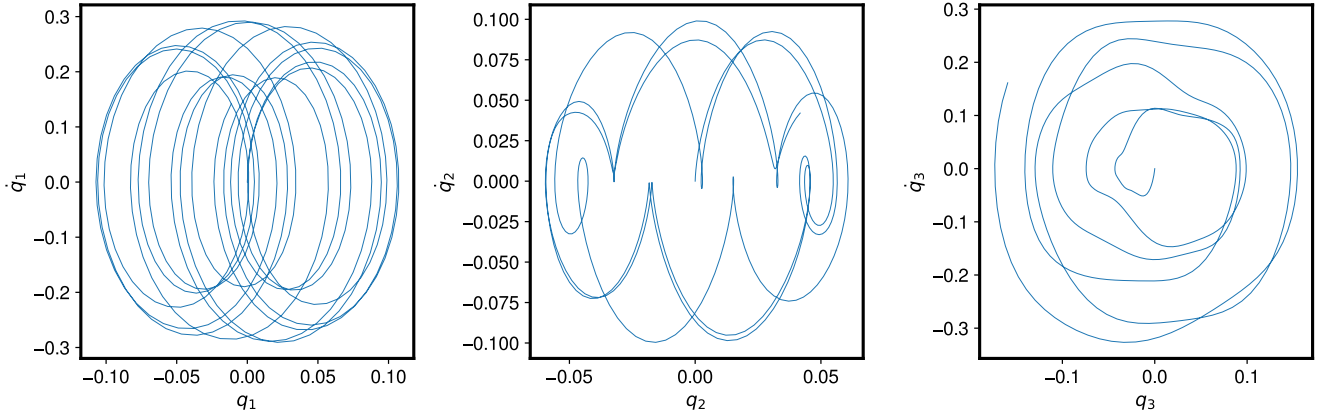


**Figure 10.** Phase portraits of the generalized coordinates of the dual-axis accelerometer for an irrotational, revolving packaging, for  $t \in [0, 20]$  seconds, and  $\gamma = 1$ .

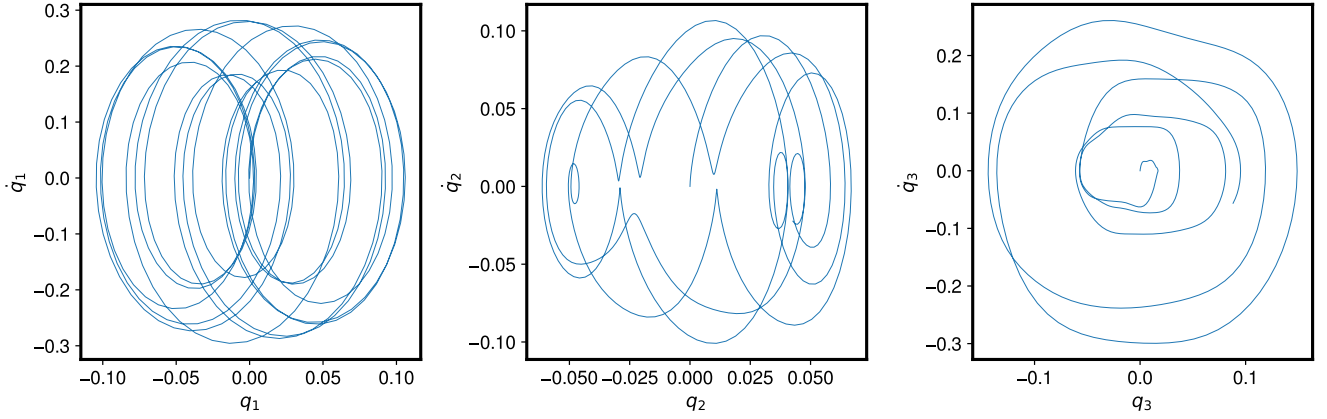


**Figure 11.** Phase portraits of the generalized coordinates of the dual-axis accelerometer for a spinning and revolving packaging, for  $t \in [0, 20]$  seconds, and  $\gamma = 1$ .

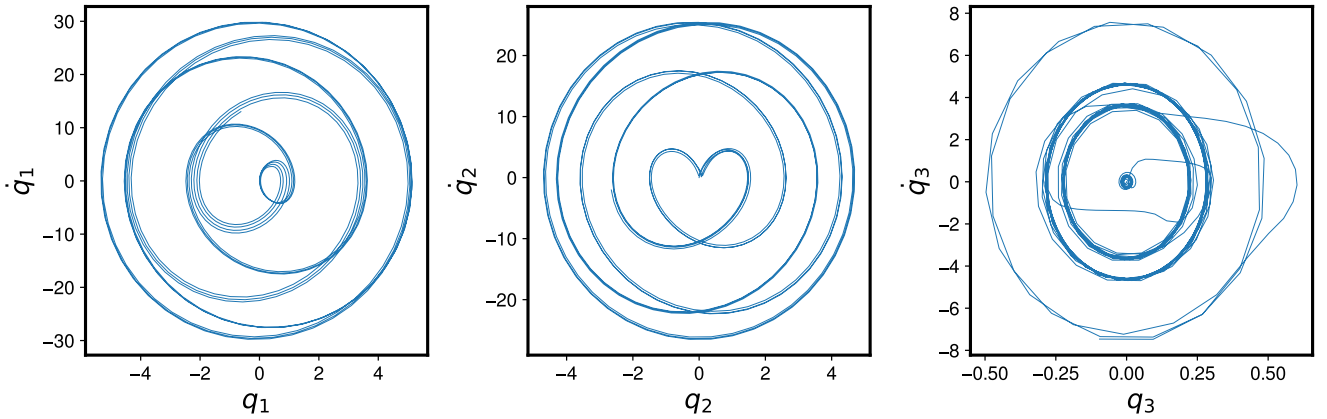


**Figure 12.** Phase portraits of the generalized coordinates of the dual-axis accelerometer for a spinning and revolving packaging, for  $t \in [0, 20]$  seconds, and  $\gamma = 5$ . Clearly, increasing  $\gamma$  from 1 to 5 lead to an increase in the maximum displacement from the equilibrium position compared to figure 11.

and only keeping terms with order less than 2, we find

$$\gamma^2 \left( \frac{\omega_0^2 - 2\lambda^2}{\omega_0^4} \right) - E \leq 0. \quad (45)$$

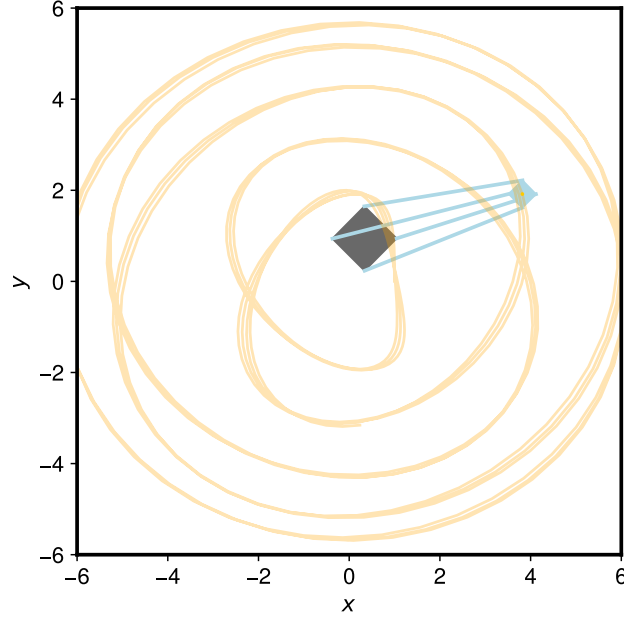


**Figure 13.** A snapshot of the dual-axis system described by figure 12 as seen in the IRF. The proof mass (shown as the blue square) is displaced well outside the packaging (shown as the gray square). The center of mass of  $m$  traces out the orange trajectory. This combination of excitations would result in failure of accelerometer.

The positive root to equation (45) gives an upper bound of  $\gamma$  such that the system remains in the linear regime:

$$\gamma_{\max} = \omega_0^2 \sqrt{\frac{N}{\omega_0^2 - 2\lambda^2}}$$

We can make a further approximation, by assuming  $\lambda \ll \omega_0$ . In this case, the upper bound of the linear operating range reduces to:

$$\gamma_{\max} = \omega_0 \sqrt{N} \quad (46)$$

Interestingly,  $\gamma_{\max} \propto 1/\lambda$ . This means that increasing the damping in the system actually reduces the optimal operating range of the accelerometer. But if we consider the extreme of tending  $\lambda \rightarrow 0$ , the time required for the oscillation of proof mass to decay would approach infinity, thus lengthening the recovery time of the accelerometer.

So far, we have neglected how one can actually measure the displacement of the proof mass from its equilibrium. Designing  $\omega_0$  to be much greater than the forcing frequency decreases the steady-state amplitude. An optimal design must balance the damping coefficient and natural frequency of the system to meet engineering constraints. Such as:

1. the minimum proof mass displacement that one can measure - this determines how sensitive the accelerometer will be to low-frequency accelerations;
2. the required operating frequency,  $\gamma_{\max}$ ;
3. the maximum recovery time;
4. the maximum cost per device and size of packaging.

By examining the dual-axis accelerometer, we realized that it is impossible to reconstruct the rotational motion of a planar rigid body using a dual-axis accelerometer alone - a MEMS gyroscope is required. This is because we can only measure the displacements of the proof mass from equilibrium ( $q_1, q_2$ ), but not its angular orientation ( $q_3$ ). As a result, we do not whether the proof mass was displaced due to translational acceleration or rotational acceleration.

Overall, the motion of the proof mass predicted by our models was intuitive and produced non-trivial insights into how the natural frequency and damping coefficient of a single-axis accelerometer might be chosen to maintain linearity.

Our results still need to be verified through experiments, or through conducting reviews of current literature on mechanical characteristics of MEMS accelerometers. To what extent our results from the single-axis model can be applied to designing a dual-axis accelerometer also remains unclear. And we did not consider the motion of the dual-axis proof mass when subjected to non-zero damping. Future work can look to:

1. verify the conclusions we drew from the single-axis model;
2. Analyze damping in the dual-axis model;
3. Develop analytical/numerical approximations of maximum operating frequency for the dual-axis model;
4. Use more realistic parameters to simulate actual MEMS accelerometers.

## 5 Conclusion

We solved for the time evolution of the proof mass for single- and dual-axis MEMS accelerometers modelled using Lagrangian mechanics. We solved the single-axis case analytically, and the dual-axis case numerically, using `python`.

Our analytical solution revealed how the natural frequency, operating frequency, and damping coefficient affect the accelerometer's mechanical characteristics. We found that increasing the natural frequency increases the maximum linear operating frequency, but the accelerometer becomes insensitive to lower frequencies. And increasing the damping coefficient shortens the recovery time, but comes at the expense of a lower maximum linear operating frequency.

The dual-axis model showed that a conventional capacitive accelerometer cannot measure rotation and justifies the need for a gyroscope to be used in conjunction to characterize the complete motion of a planar rigid body.

## Acknowledgement

Thank you, Mona (Prof. Berciu) for a great term ★.

## References

1. Mohammed, Z., Elfadel, I. & Rasras, M. Monolithic multi degree of freedom (mdof) capacitive mems accelerometers. *Micromachines* **9**, 602, DOI: [10.3390/mi9110602](https://doi.org/10.3390/mi9110602) (2018).
2. Hughes, M. Low-noise, wide-bandwidth: A single axis analog accelerometer from analog devices (2018).
3. Petsch, K. & Kaya, T. Design, fabrication, and analysis of mems three-direction capacitive accelerometer (2012).
4. Landau, L. D. & Lifshitz, E. M. *Mechanics, Third Edition: Volume 1 (Course of Theoretical Physics)* (Butterworth-Heinemann, 1976), 3 edn.
5. Boas, M. L. *Mathematical methods in the physical sciences; 3rd ed.* (Wiley, Hoboken, NJ, 2006).